RSC Advances

PAPER

View Article Online
View Journal | View Issue



Cite this: *RSC Adv.*, 2026, **16**, 18938

# An injectable photo-crosslinking silk hydrogel system with biphasic release of BTXA and 5-Fu promotes scarless wound healing

Ming Xu,†[ab] Xihang Wang,†[c] Ziyi Zhou,†[a] Linna Wang,[d] Jia Zhou,[d] Xinyue Hu,[a] Yuanfei Wang*[e] and Tong Wu *[ab]

Hypertrophic scarring is characterized by excessive dermal fibrosis and irregular collagen metabolism, mediated by fibroblasts derived from keloids. This condition typically arises from improper wound healing after deep burns, trauma, or surgical procedures. Although intralesional injections of botulinum toxin type A and 5-fluorouracil are common clinical treatments, their effectiveness is often limited by temporary drug retention, insufficient penetration depth, and complications from repeated injections. To overcome these challenges, we developed an injectable composite hydrogel system, F@P-B-SilMA, to promote scarless wound healing. Systematic characterization revealed that this system undergoes rapid UV-initiated *in situ* polymerization and exhibits a three-dimensional porous microstructure. It also demonstrates excellent tissue adhesion and mechanical compliance, along with favorable rheological properties, and tunable degradation kinetics that align with the various phases of wound healing. These attributes collectively meet the essential criteria for advanced wound dressings. Comprehensive *in vitro* and *in vivo* evaluations confirmed the system's biocompatibility and its dual ability to accelerate wound closure while suppressing fibrotic proliferation. The injectable F@P-B-SilMA composite hydrogel system represents a promising therapeutic approach for clinical scar management, showcasing significant potential as a next-generation wound dressing for scarless tissue regeneration.

Received 27th December 2025
Accepted 1st April 2026

DOI: 10.1039/d5ra10037b

rsc.li/rsc-advances



## 1. Introduction

Hypertrophic scarring (HS) typically arises from abnormal wound healing following deep burns, trauma, or surgical procedures. Clinically, it manifests as overproduction of dermal tissue and dysregulation of collagen metabolism, driven by fibroblasts derived from the scar.[1] Global epidemiological data show that approximately 100 million people develop cutaneous scars each year due to surgical or traumatic injuries, and about 15% of these cases progress to hypertrophic scars or keloids at the original wound sites.[2] In addition to cosmetic issues, HS often causes chronic pain, itching, structural deformities, and problems with tissue function.[3] Current therapeutic modalities including surgical excision, laser therapy, and radiotherapy[4–6] present distinct limitations: surgical interventions carry risks of secondary trauma and high costs, laser treatment demonstrates significant recurrence rates, and radiotherapy poses potential adverse effects.[7–9] Clinical evidence supports the use of intralesional drug injections as a minimally invasive and cost-effective strategy for managing scars.[10–13]

Botulinum toxin type A (BTXA) has been a major area of research since it received U.S. Food and Drug Administration (FDA) approval for use in medical aesthetics in 2002. Clinicians have demonstrated its safety and effectiveness in managing pathological scarring.[14] Research shows that early prophylactic BTXA administration at wound sites improves tissue repair quality, highlighting its potential as a targeted intervention for reducing pathological scarring.[15,16] Despite its potential, treatment-related complications such as injection pain, localized side effects, and poor patient adherence have limited the wider clinical use of scar modulation therapies. At the same time, 5-fluorouracil (5-Fu) continues to be a key antimetabolite for treating pathological scarring, functioning through two main mechanisms: inhibiting fibroblast proliferation and reducing collagen synthesis.[17] However, pharmacokinetic limitations remain: rapid systemic clearance (short plasma half-life) and limited penetration into scar tissue significantly reduce drug bioavailability at the injection site.[18] Additionally, long-

[a]*Medical Research Center, The Affiliated Hospital of Qingdao University, Qingdao Medical College, Qingdao University, Qingdao 266000, China. E-mail: twu@qdu.edu.cn*

[b]*Shandong Key Laboratory of Medical and Health Textile Materials, Collaborative Innovation Center for Eco-textiles of Shandong Province and the Ministry of Education, College of Textile & Clothing, Qingdao University, Qingdao 266071, China*

[c]*Department of Plastic Surgery, Qilu Hospital (Qingdao), Shandong University, Qingdao 266035, China*

[d]*Lanzhou Biotechnique Development Co., Ltd, Lanzhou 730046, China*

[e]*Qingdao Stomatological Hospital Affiliated to Qingdao University, Qingdao 266001, China. E-mail: wangyuanfei@qdu.edu.cn*

† Ming Xu, Xihang Wang, and Ziyi Zhou contributed equally to this work.

term high-dose treatments can lead to serious complications, including ulcerative lesions, ongoing pain, and pathological hyperpigmentation.[19,20] These pharmacological challenges highlight the urgent need for innovative delivery methods to improve drug retention, optimize biodistribution, and reduce complications associated with injection frequency in scar therapeutics.

In recent years, nanotechnology and biomaterials have advanced rapidly in the field of wound repair and tissue regeneration,[21–24] and the development of advanced biological dressings for scarless wound healing has become a key research direction in tissue engineering.[25–28] Silk fibroin (SF) is a natural biopolymer obtained from the cocoons of *Bombyx mori*, and it is a crucial component in hydrogel fabrication due to its remarkable biomimetic properties.[29] Recent advancements in injectable hydrogel systems utilize their three-dimensional porous structure, adjustable mechanical properties, and characteristics resembling the natural extracellular matrix (ECM) to function as versatile platforms for drug delivery and cellular support in wound regeneration.[30] Methacrylated silk fibroin (SilMA), created by modifying silk fibroin with glycidyl methacrylate, shows excellent tissue adhesion and quick photocuring under UV light, making it an ideal biomaterial for managing wound interfaces.[31,32] Building on these advancements, poly(lactic-*co*-glycolic acid) (PLGA) provides controlled drug release dynamics and scaffold compatibility for tissue engineering applications.[33] Studies using coaxial electrospray technology have successfully created paclitaxel (PTX)-encapsulated calcium alginate-PLGA composite microspheres. These microspheres demonstrate sustained drug release patterns that improve localized therapeutic efficacy while reducing systemic exposure and dosing frequency.[34] Therefore, the utilization of coaxial electrospray technology for drug encapsulation establishes a novel paradigm to achieve sustained therapeutic release profiles while mitigating systemic toxicity in pharmacological interventions.

To address these challenges, we developed an innovative injectable hydrogel composite system that combines BTXA with 5-Fu@PLGA microspheres embedded in a hydrogel matrix to promote scarless wound healing. Our systematic approach began with initial screenings to identify the optimal concentrations of 5-Fu and BTXA for cellular applications. After optimization, we designed core–shell structured microspheres of 5-Fu@PLGA using electrostatic spray technology. We then strategically incorporated these drug-loaded microspheres into SilMA hydrogels that had previously been injected with BTXA. The resulting composite was thoroughly evaluated for performance indicators and biocompatibility to ensure its safety and efficacy. To assess the therapeutic potential of this hydrogel system, we developed a rabbit ear scar model for *in vivo* evaluation. In the early stages of wound healing, the composite hydrogel was directly photocured *in situ* within the wound. During this phase, the SilMA hydrogel component loaded with BTXA served as an active dressing, creating optimal conditions for accelerated wound closure while preventing the initial formation of excessive scarring. As the healing process progressed into the later stages, our system design enabled the controlled degradation of the 5-Fu@PLGA shell and core-structured microspheres. This degradation mechanism allowed for the sustained release of 5-Fu, targeting the already formed scar tissue and prolonging the therapeutic effect. The timing of the action between the two bioactive ingredients—BTXA, which acts early, and 5-Fu, which acts later—creates a synergistic effect specifically aimed at eliminating hyperplastic scarring. This biphasic delivery method effectively addresses the various phases of the wound healing process, ultimately promoting scarless healing.

## 2. Materials and methods

### 2.1 Materials

BTXA was provided by Lanzhou Biotechnology Development Co., Ltd (Lanzhou, China); 5-Fu (purity ≥ 99%) and fluorescein-labeled bovine serum albumin (FITC-BSA) were purchased from Sigma-Aldrich Co. Ltd; PLGA (PLA : PGA = 10 : 90) was purchased from Shenzhen Match Biomaterials Co. Ltd; hexafluoroisopropanol (HFIP) was purchased from Shanghai Darui Chemical Co. Ltd; methacryloylated silk fibroin (SilMA) and lithium phenyl (2,4,6-trimethylbenzoyl) phosphinate (LAP) were purchased from Engineering For Life (Suzhou, China); rhodamine (RB) was purchased from Macklin Biochemical Technology Co., Ltd (Shanghai, China); Cell Counting Kit-8 (CCK-8) was purchased from Aladdin Biochemical Science and Technology Co., Ltd (Shanghai, China); Phalloidin-iFlour 488™, DAPI, lidocaine and 4% paraformaldehyde were purchased from Beijing Solarbio Science & Technology Co., Ltd (Beijing, China); isoflurane were purchased from RWD Life Science Co., Ltd (Beijing, China); Hematoxylin-Eosin (H&E) staining solution and Masson's trichrome staining solution were purchased from Zhuhai Baso Biotechnology Co., Ltd (Zhuhai, Guangdong, China); α-SMA (67735-1-Ig), Col-I (66761-1-Ig) and Col-III (68320-1-Ig) monoclonal antibodies were purchased from Proteintech Group, Inc (Wuhan, China).

### 2.2 Cell culture

The Human Keloid Fibroblast cells (HKFs) used in this experiment were provided by the Department of Medical Aesthetics at The Affiliated Hospital of Qingdao University (Qingdao, China). The mouse fibroblast (L929) cells were obtained from Prosperity Life Sciences Co., Ltd (Wuhan, China). Both cell types were cultured in DMEM medium supplemented with 10% fetal bovine serum and 1% penicillin–streptomycin. Cells were maintained at 37 °C under a humidified atmosphere of 5% $CO_2$ and 70–80% relative humidity. Cells in the logarithmic growth phase were harvested for subsequent experiments.

### 2.3 Cell proliferation assay *in vitro*

HKFs and L929 cells were uniformly seeded in 96-well plates at a density of $5 \times 10^3$ cells per well and incubated for 24 hours. After this incubation period, the cells were treated with varying concentrations of BTXA (0, 0.2, 0.4, 0.8 U) or 5-Fu (0, 12.5, 25.0, 50.0, 100.0, 200.0 μg $mL^{-1}$), which were diluted in complete medium. The treatments were conducted over 1, 3, and 5 days.

Cell viability was assessed using the CCK-8 kit according to the manufacturer's protocol, with absorbance measured at 450 nm. Statistical analysis and the calculation of the half-maximal inhibitory concentration ($IC_{50}$) for 5-Fu were performed using GraphPad Prism.

### 2.4 Cell morphology staining

HKFs and L929 cells were seeded into 24-well plates at a density of $5 \times 10^3$ cells per well and co-cultured for 3 days in mixed media, according to the BTXA and 5-Fu groupings described in the aforementioned *in vitro* cell proliferation assay. After fixation with 4% paraformaldehyde for 15 minutes and washing with PBS, the cells were permeabilized with 0.1% Triton X-100 for 10 minutes at room temperature, followed by another PBS wash. Immunofluorescence staining was performed using Alexa Fluor 488™ diluted in 1% BSA, with a 1 hour incubation in the dark, followed by three washes with PBS. The nuclei were counterstained with DAPI (1 μM) for 10 minutes in the dark. Fluorescent images were captured using an inverted microscope.

### 2.5 Preparation and characterization of 5-Fu@PLGA microspheres

Core-shell structured microspheres of 5-Fu@PLGA were fabricated *via* coaxial electrospraying. The core solution contained 5-Fu (1 mg $mL^{-1}$) dissolved in deionized water, while the shell solution comprised 5% (w/v) PLGA dissolved in HFIP. The electrospray parameters were optimized as follows: the flow rates for the core and shell solutions were set at 0.33 mL $h^{-1}$ and 1.0 mL $h^{-1}$, respectively. An applied voltage of +20 kV was used for the nozzle, −5 kV for the collector, and the working distance was maintained at 12 cm.

To fabricate 5-Fu@PLGA microspheres with a core–shell structure, FITC-BSA (green fluorescence) was incorporated into the core layer, while RB (red fluorescence) was incorporated into the shell layer. The microspheres were placed on a glass slide and observed using a fluorescence microscope. Scanning electron microscopy (SEM) was employed to analyze the particle size, morphology, and homogeneity of the microspheres. 50 randomly selected microspheres were used to quantify particle size distribution using ImageJ. *In vitro* drug release kinetics of 5-Fu@PLGA microspheres were evaluated at 265 nm using a multimode microplate reader (Varioskan LUX, Thermo Fisher Scientific, Waltham, MA, USA).

### 2.6 Preparation and characterization of the hydrogel systems

The SilMA hydrogel was prepared according to the manufacturer's protocol. In brief, 0.25 g of SilMA was dissolved in 1 mL of LAP photoinitiator solution and magnetically stirred at room temperature for 30 minutes. Next, 0.2 U of BTXA and a specified number of 5-Fu@PLGA microspheres were added to the SilMA precursor. This mixture underwent vortex treatment followed by ultrasonic treatment for 5 minutes to ensure complete dispersion. Four hydrogel formulations were then photocured under 405 nm light irradiation: SilMA, BTXA-SilMA (B-SilMA), 5-Fu@PLGA-SilMA (F@P-SilMA), and 5-Fu@PLGA-BTXA-SilMA (F@P-B-SilMA).

The adhesiveness and flexibility of the hydrogel were evaluated using a digital camera to capture its conformal attachment to the periarticular skin of the hand. Rheological characterization was conducted with a rotational rheometer. For structural analysis, freeze-dried hydrogels were sectioned, coated with gold, and imaged using SEM. Pore size distribution was quantified using ImageJ software. To assess the swelling behavior, cured hydrogels (initial mass $m_0$) were incubated in PBS under physiological conditions (37 °C, 100 rpm shaking). At predetermined intervals, samples were removed, surface-blotted with filter paper, and weighed ($m_1$) to calculate mass retention. The degradation rate can be calculated using the following equation:

$$\text{degradation}(\%) = \frac{m_0 - m_1}{m_0} \times 100$$

### 2.7 Evaluation of *in vitro* biosafety and therapeutic efficacy of hydrogel systems

Hydrogels from various experimental groups were incubated in a complete medium using a shaker at 37 °C for 24 hours to prepare extracts. The control group received complete medium alone, while the experimental groups received SilMA, B-SilMA, F@P-SilMA, and F@P-B-SilMA hydrogel extracts. The effects of these extracts on cell proliferation were evaluated using HKFs and L929 cells, as outlined in Section 2.3.

### 2.8 Construction of hypertrophic scar model in the rabbit ear *in vivo*

Adult male New Zealand White rabbits (2.0–2.5 kg, supplied by Qingdao Kondebio Biotechnology Co., Ltd) underwent the following procedures: the ventral auricular surfaces were depilated, disinfected, and surgically prepared. Combined anesthesia comprising lidocaine local injection and isoflurane inhalation was administered. Five full-thickness circular wounds (10 mm diameter) were created per ear using a biopsy punch, symmetrically aligned along the median auricular axis with ≥10 mm spacing. The perichondrium was meticulously removed with a cartilage separator, ensuring cartilage integrity. Animals were randomly allocated to five groups: Control, SilMA, B-SilMA, F@P-SilMA, and F@P-B-SilMA. Hydrogel formulations were then injected into the wounds and photocrosslinked *in situ* using 405 nm light for 25 seconds. The wounds were secured with 3M transparent dressings. The wounds in the control group received only petroleum jelly. Pre- and postoperative wound documentation was carried out using standardized imaging techniques. All procedures adhered to the animal care protocols approved by the Qingdao University Animal Ethics Committee (no. 20250103NZB0520250203013).

### 2.9 Effects of different hydrogels on wound healing and scar formation *in vivo*

Wound healing progress was monitored on postoperative days 1, 3, 7, 14, and 21. Standardized photographs were taken at each

time point, and wound areas were quantified using ImageJ software. The healing rate (%) was calculated as follows:

$$\text{wound closure}(\%) = \frac{\text{wound area on day 0} - \text{wound area on day 14}}{\text{wound area on day 0}} \times 100$$

Specimens were collected from rabbit ears on postoperative day 21, which included 2 mm of peri-wound tissue along with adjacent normal skin (referred to as the normal group). Following fixation in 4% paraformaldehyde, the tissues were processed through graded ethanol dehydration and then embedded in paraffin. Serial sections measuring 5 μm in thickness were prepared using a frozen sectioning machine (Leica, Germany). These sections underwent various staining procedures, including H&E, Masson, and immunohistochemistry (IHC). The primary antibodies utilized for IHC included α-SMA (1 : 200), Col-I (1 : 400), and Col-III (1 : 600). ImageJ software was used to quantify the epidermal thickness index (ETI), scar proliferation index (SEI), and protein expression levels across different subgroups. The formula for these calculations was as follows:

$$\text{SEI} = \frac{\text{height of scar tissue}}{\text{height of the adjacent normal skin}}$$

SEI = 1 indicates that the thickness of dermal regeneration in the wound corresponds to normal tissue without scar formation. SEI > 1 signifies dermal hyperplasia and a diagnosis of HS.

$$\text{ETI} = \frac{\text{thickness of scar tissue epidermis}}{\text{thickness of normal skin epidermis}}$$

ETI = 1 indicates that the thickness of epidermal regeneration is consistent with normal tissue, suggesting no scar formation. ETI > 1 indicates abnormal epidermal thickening, which suggests epidermal hyperplasia.

### 2.10 Statistical analysis

All data are presented as mean ± standard deviation ($x \pm$ SD). The experiments were statistically analyzed using GraphPad Prism 9.0 software. Differences between the two groups were assessed using Student's *t*-test, while comparisons involving three or more groups were analyzed using one-way ANOVA. Error bars represent the standard deviation of three measurements in each group, and Tukey's test was employed as a post-hoc analysis method. Differences were deemed statistically significant if $P < 0.05$.

## 3. Results and discussion

### 3.1 Screening of 5-Fu drug concentrations

5-FU, a commonly used antimetabolite, is effective in treating malignant tumors. The therapeutic effects of this drug and its associated toxicity risks are significantly bidirectional.[19] On one hand, 5-FU effectively inhibits the over-proliferation of keloid fibroblasts by disrupting DNA and RNA synthesis.[35] On the other hand, it may harm the highly metabolically active normal keratinocytes. To evaluate the safe and effective concentration of 5-Fu[18] (12.5, 25, 50, 100, and 200 μg mL$^{-1}$) on the viability of HKFs and L929 cells, the CCK-8 assay was used. The results indicated that varying concentrations of 5-Fu had a significant inhibitory effect on L929 cell viability compared with the Control group ($P < 0.05$). As the concentration of 5-Fu increased, the cell viability gradually decreased (Fig. 1a). Similarly, for HKFs, different concentrations of 5-Fu significantly reduced cell viability ($P < 0.001$). The higher the concentration, the more pronounced the inhibitory effect, demonstrating a dose–response relationship of 5-Fu on HKF cells (Fig. 1b). On the fifth day of observation, there was no significant difference in cell viability for L929 at concentrations ranging from 12.5 to 50 μg mL$^{-1}$. However, a significant decrease in HKF viability was observed, with 50 μg mL$^{-1}$ proving particularly effective at inhibiting these cells ($P < 0.05$). The half-inhibitory concentrations ($IC_{50}$) of 5-Fu for both L929 cells and HKFs were calculated based on the optical density (OD) values from the CCK8 assay on the fifth day. The results indicated that the $IC_{50}$ of 5-Fu was significantly lower in HKFs than in L929 cells, at 73.05 μg mL$^{-1}$ and 3.56 μg mL$^{-1}$, respectively. This suggests that HKFs are more sensitive to 5-Fu than L929 cells (Fig. S1). Additionally, cell morphology staining was conducted to assess the effects of varying concentrations of 5-Fu on the morphology of HKFs and L929 cells. The staining results showed that, compared with the control group, HKFs contracted and lost their characteristic spreading morphology as the 5-Fu concentration increased. In contrast, the morphology of L929 cells did not exhibit significant changes (Fig. 1c and d). In conclusion, based on the principles of drug efficacy and safety, a concentration of 50 μg mL$^{-1}$ of 5-Fu was selected for subsequent experiments.

### 3.2 Screening of BTXA drug concentrations

BTXA is a potent neurotoxin produced by the Gram-positive bacterium *Clostridium botulinum*.[36] It shows promising therapeutic potential for HS. While the exact mechanism by which it reduces scarring is not fully understood, current theories suggest it modulates scar mechanical tension through localized muscle relaxation. This relaxation may indirectly influence fibroblast activity, helping to reduce scar proliferation.[37–40] Similar to 5-Fu, we examined the effects of BTXA at concentrations of 0.2 U, 0.4 U, and 0.8 U on the viability of HKFs and L929 cells using the CCK-8 assay. The results indicated that BTXA at different concentrations inhibited L929 cell proliferation compared with the control group ($P < 0.05$). Furthermore, the inhibitory effect became more pronounced with higher concentrations (Fig. 2a). In HKFs, the BTXA concentrations showed a more significant reduction in cell viability ($P < 0.001$), with increased concentration leading to greater inhibition (Fig. 2b). Cytomorphological staining results revealed that varying concentrations of BTXA did not lead to significant morphological changes in HKFs and L929 cells compared with the control group (Fig. 2c and d). Based on the principles of

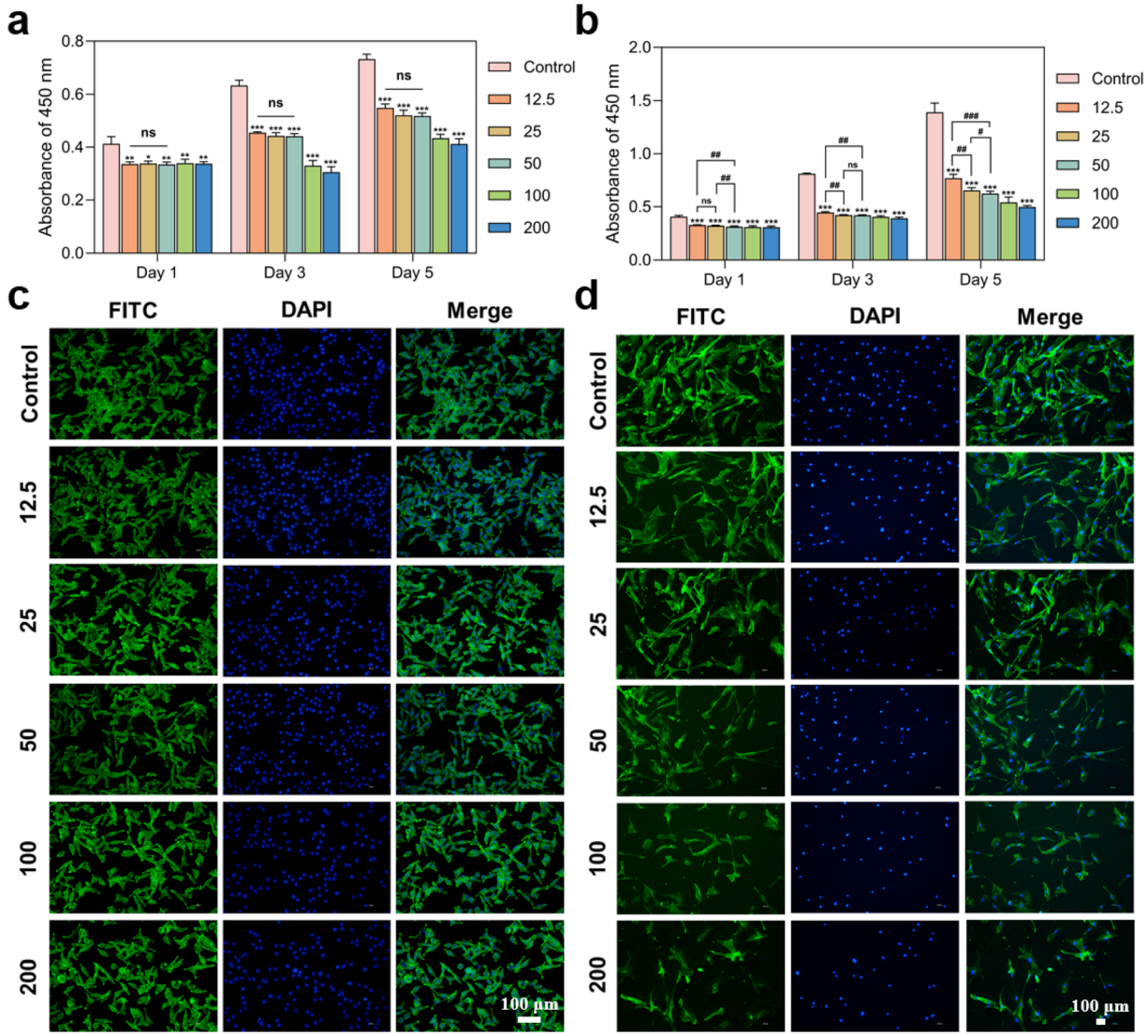


Fig. 1 Screening of 5-Fu drug concentrations. (a) L929 cell viability and (b) HKFs viability after treatment with different concentrations of 5-Fu. Morphology staining of (c) L929 cells and (d) HKFs after treated with different 5-Fu concentrations (0, 12.5, 25, 50, 100, and 200 μg $mL^{-1}$). "ns" indicates no significant difference between groups. ***$P$ < 0.001, **$P$ < 0.01, and *$P$ < 0.05 indicate statistically significant difference when compared with the control group. $^{###}P$ < 0.001, $^{##}P$ < 0.01, and $^{#}P$ < 0.05 indicate statistically significant difference between the compared groups.

drug efficacy and safety, we selected 0.2 U of BTXA for subsequent experiments.

### 3.3 Preparation and characterization of 5-Fu@PLGA and F@P-B-SilMA

Currently, the clinical application of 5-Fu for scar prevention and treatment primarily involves intralesional multiple injections and wound irrigation. However, its short half-life *in vivo*, the need for repeated injections, and the risk of delayed wound healing limit its application in scar management. To overcome the current limitations of 5-Fu in the treatment of HS, we developed core–shell structured 5-Fu@PLGA microspheres *via* coaxial electrospraying (Fig. 3a). This sustained-release system is designed to prolong drug release, enhance therapeutic efficacy, and reduce side effects. To verify this structure, fluorescence staining was employed for characterization. The merged fluorescence images revealed that the 5-Fu core layer loaded with FITC-BSA was encapsulated by the PLGA shell layer containing RB, forming a well-defined distinct core–shell structure, indicating the successful fabrication of core–shell structured 5-Fu@PLGA microspheres *via* electrospray technology (Fig. S2). SEM imaging showed that the microspheres exhibited a spherical shape with uniform morphology and size distribution (Fig. 3b). Particle size analysis indicated a predominant diameter of approximately 1 μm (Fig. S3). Collectively, these results confirm the successful preparation of the core–shell structured microspheres. *In vitro* drug release profiling, performed *via* UV-vis spectroscopy, demonstrated biphasic kinetics: an initial burst release of 45.29 ± 1.88% within 4 hours, followed by a sustained release of 58.90 ± 4.60%

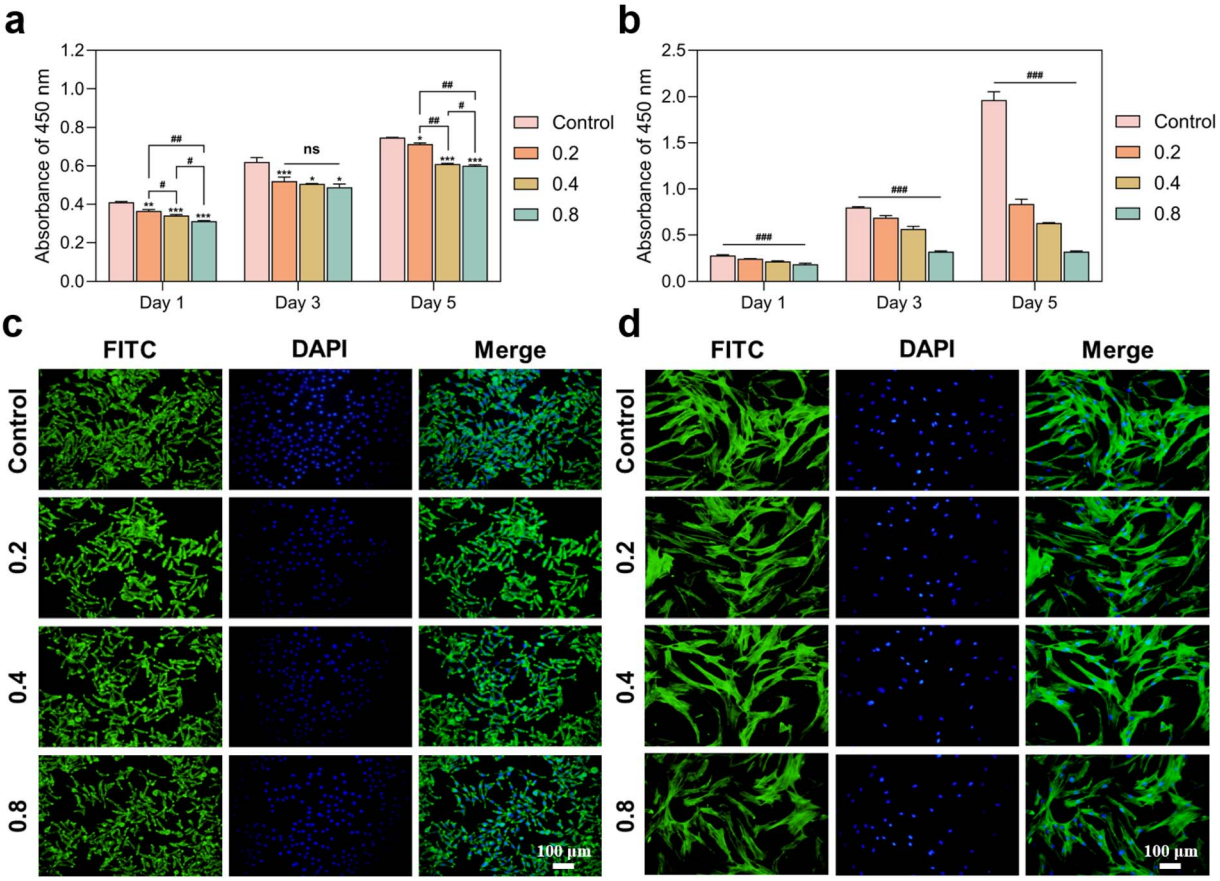


Fig. 2 Screening of BTXA drug concentrations. (a) L929 cell viability and (b) HKFs cell viability after treatment with different concentrations of BTXA. Morphology staining of (c) L929 cells and (d) HKFs after treated with different BTXA concentrations (0, 0.2, 0.4, and 0.8 U). "ns" indicates no significant difference between groups. ***$P < 0.001$, **$P < 0.01$, and *$P < 0.05$ indicate statistically significant difference when compared with the control group. $^{\#\#\#}P < 0.001$, $^{\#\#}P < 0.01$, and $^{\#}P < 0.05$ indicate statistically significant difference between the compared groups.

cumulatively at 72 hours, ultimately reaching 65.59 ± 4.23% over 20 days (Fig. 3c). This release profile validates the system's capabilities for sustained delivery, which is characteristic of long-acting formulations.

Digital imaging illustrates the sequential gel testing of periarticular finger skin as it transitions from a liquid to a solid state. The photocured SilMA hydrogel maintained its structural integrity during bending, stretching, and manual manipulation, showcasing excellent adhesive and deformable properties (Fig. 3d). Rheological analysis confirmed the successful formation of the SilMA hydrogel: UV irradiation at 405 nm initiated gelation within 10 seconds, with the storage modulus ($G'$) surpassing the loss modulus ($G''$) between 90 and 100 seconds. This indicates a complete transition from liquid to gel and highlights the rapid *in situ* photocrosslinking capability (Fig. S4). The incorporation of 5-Fu@PLGA microspheres and 0.2 U BTXA into the SilMA precursor solution allowed for comparative SEM analysis of the freeze-dried hydrogels. Both SilMA and F@P-B-SilMA exhibited three-dimensional reticulated porous architectures. Notably, F@P-B-SilMA displayed greater surface roughness and visible 5-Fu@PLGA microspheres within its pore spaces (Fig. 3e).

As demonstrated in Fig. 3f and S5, pore size analysis revealed that the F@P-B-SilMA composites had smaller pore diameters and increased microporosity compared to SilMA ($P < 0.001$). This interconnected network structure enhances wound-dressing applications by absorbing exudate, maintaining moisture balance, and promoting cellular adhesion and growth, while allowing therapeutic loading of drugs, cells, and microspheres to inhibit scarring.[41,42] The hydrogels exhibited suitable biodegradability and degradation rates for tissue engineering applications.[30] Fig S6 demonstrates that incorporating 5-Fu@PLGA and BTXA modified the degradation profiles of the composite hydrogels to varying degrees. However, these differences were not statistically significant. The degradation time for all hydrogels exceeded two weeks, providing adequate degradation capacity to align with the timeframe required for wound healing. The CCK-8 assay was used to evaluate the *in vitro* biocompatibility of the composite hydrogels and their inhibitory effect on HFKs. The results showed comparable cell viability across the hydrogel groups and controls on days 1 and 3, with viability remaining above 90%, despite a slight decline by day 5 (Fig. 3g). Additionally, as demonstrated in Fig. 3h, SilMA did not have a significant inhibitory effect on HFKs compared to the control group ($P < 0.01$). In contrast, the

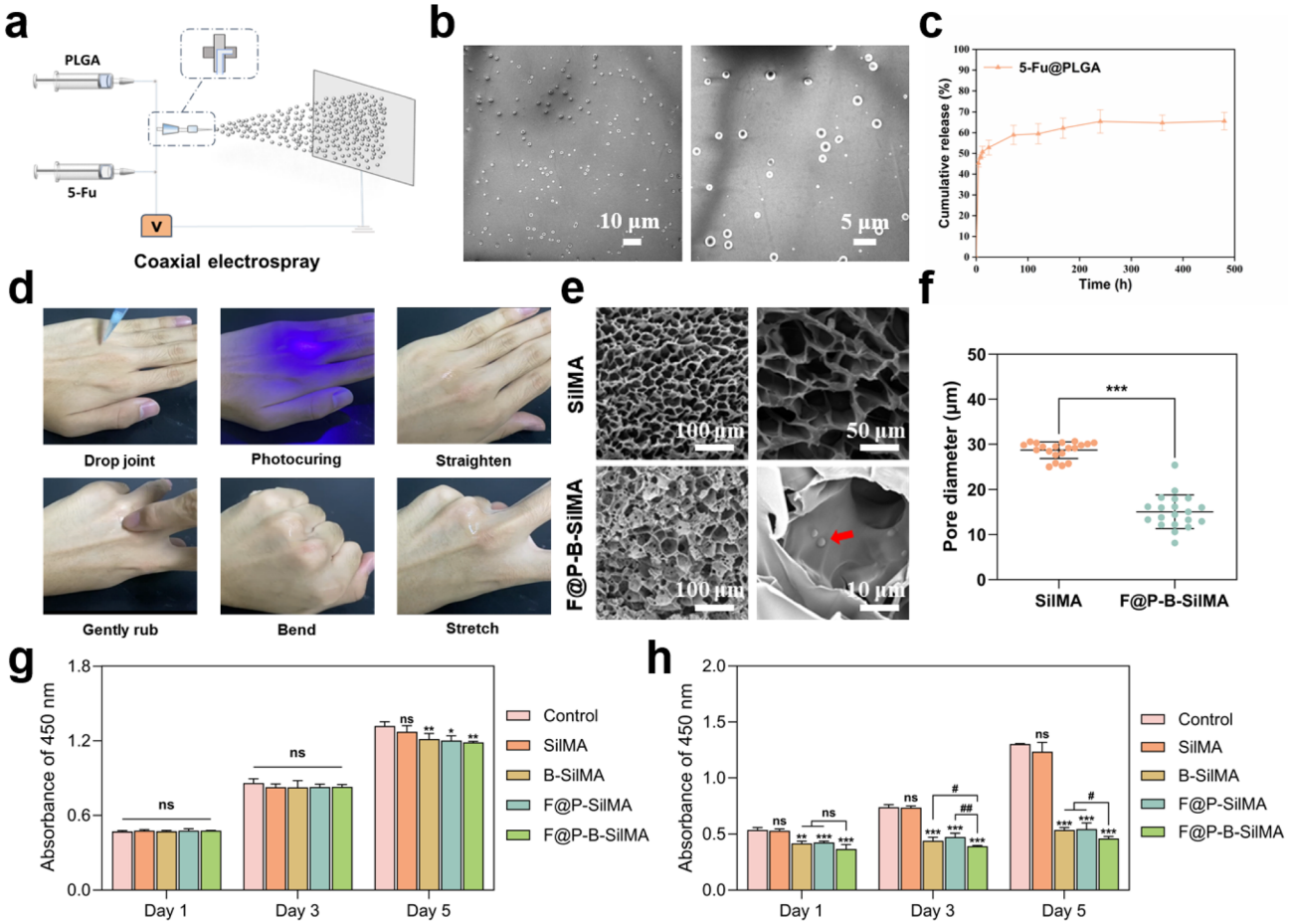


Fig. 3 Preparation and characterization of 5-Fu@PLGA and F@P-B-SilMA. (a) Schematic illustration of microsphere preparation. (b) SEM images of 5-Fu@PLGA microspheres at different magnifications. (c) Cumulative drug release profile of 5-Fu. (d) Flexural adhesion testing of SilMA hydrogel on periarticular skin. (e) SEM images of SilMA and F@P-B-SilMA hydrogels. (f) Comparative pore size analysis of SilMA and F@P-B-SilMA. Viability of (g) L929 and (h) HKFs cells after culture with extracts from the different groups. "ns" indicates no significant difference between groups. ***$P < 0.001$, **$P < 0.01$, and *$P < 0.05$ indicate statistically significant difference when compared with the control group. $^{\#\#}P < 0.01$ and $^{\#}P < 0.05$ indicate statistically significant difference between the compared groups.

hydrogel containing 5-Fu@PLGA and BTXA significantly inhibited HFKs, with the inhibition rates of F@P-B-SilMA on days 3 and 5 showing better performance than those of B-SilMA and F@P-SilMA ($P < 0.05$). These findings indicate that F@P-B-SilMA exhibits good cytocompatibility and an inhibitory effect on HFKs; the latter may be attributed to the sustained release of BTXA and 5-Fu from the composite hydrogel system, warranting further *in vivo* evaluation.

### 3.4 F@P-B-SilMA promotes wound healing *in vivo*

Due to limitations in rat models for excessive scar proliferation, a rabbit ear model that mimics human pathophysiology of proliferative scarring has been established.[43] Following established methodologies,[44–46] full-thickness skin wounds were created in rabbit ears. The effectiveness of the F@P-B-SilMA composite hydrogel in promoting wound healing was evaluated for the first time. Various hydrogel formulations (SilMA, B-SilMA, F@P-SilMA, and F@P-B-SilMA) were applied to the wounds *in situ* and photocured using 405 nm ultraviolet light to ensure proper adhesion, while the control group received petroleum jelly treatment (Fig. 4a). Wound healing progression was documented using digital photography on days 0, 1, 3, 7, 14, and 21 post-treatment, and wound quantification was performed using statistical software. The results showed a significantly greater reduction in wound area in the hydrogel-treated groups compared to controls during the regeneration phase (Fig. 4b and c). Notably, the hydrogel groups showed accelerated healing rates from day 0 to day 14. This improvement may be attributed to SilMA's beneficial biological properties, which enhance wound healing by increasing fibroblast proliferation and matrix deposition and decreasing inflammatory responses.[47] By day 14, the wound healing rate in the hydrogel groups was superior to that in the control group ($P < 0.05$), and no significant differences were observed among the SilMA, B-SilMA, F@P-SilMA, and F@P-B-SilMA groups (Fig. S7). At day 21, we also observed the condition of the scars formed in the different groups. As illustrated in Fig. 4b, the F@P-B-SilMA group showed the best results, with scar coloration closely resembling that of the adjacent normal skin. Additionally, this

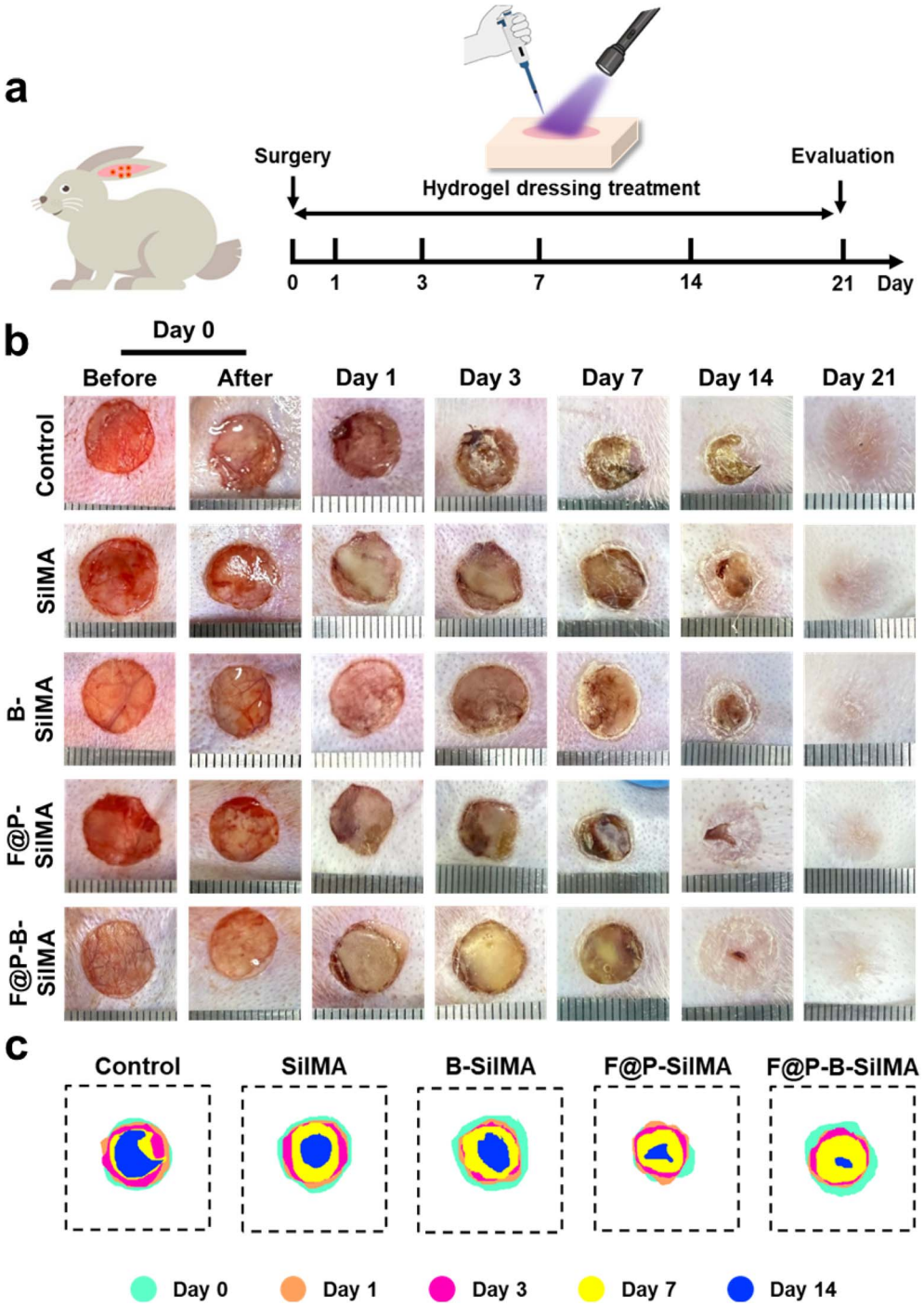


Fig. 4 F@P-B-SilMA promotes wound healing *in vivo*. (a) Schematic of experimental design and *in situ* hydrogel photocuring at wound sites. (b) Representative photographs showing wound healing process after treatment by the different groups at designated time points. (c) Diagrams of the dynamic wound healing process.

group had significantly reduced scar thickness and improved pliability compared to the other groups.

### 3.5 Histological staining analysis of HS inhibition by F@P-B-SilMA

To evaluate the therapeutic potential of the F@P-B-SilMA hydrogel in reducing HS during wound healing, we collected scar tissue samples from rabbit ears on day 21 for histological analysis. We used H&E and Masson staining, with adjacent normal skin serving as controls. The H&E staining revealed significant thickening of the epidermis and dermis, along with HS formation, across all treatment groups compared with normal tissue. Notably, the specimens treated with F@P-B-SilMA showed the closest histological resemblance to normal

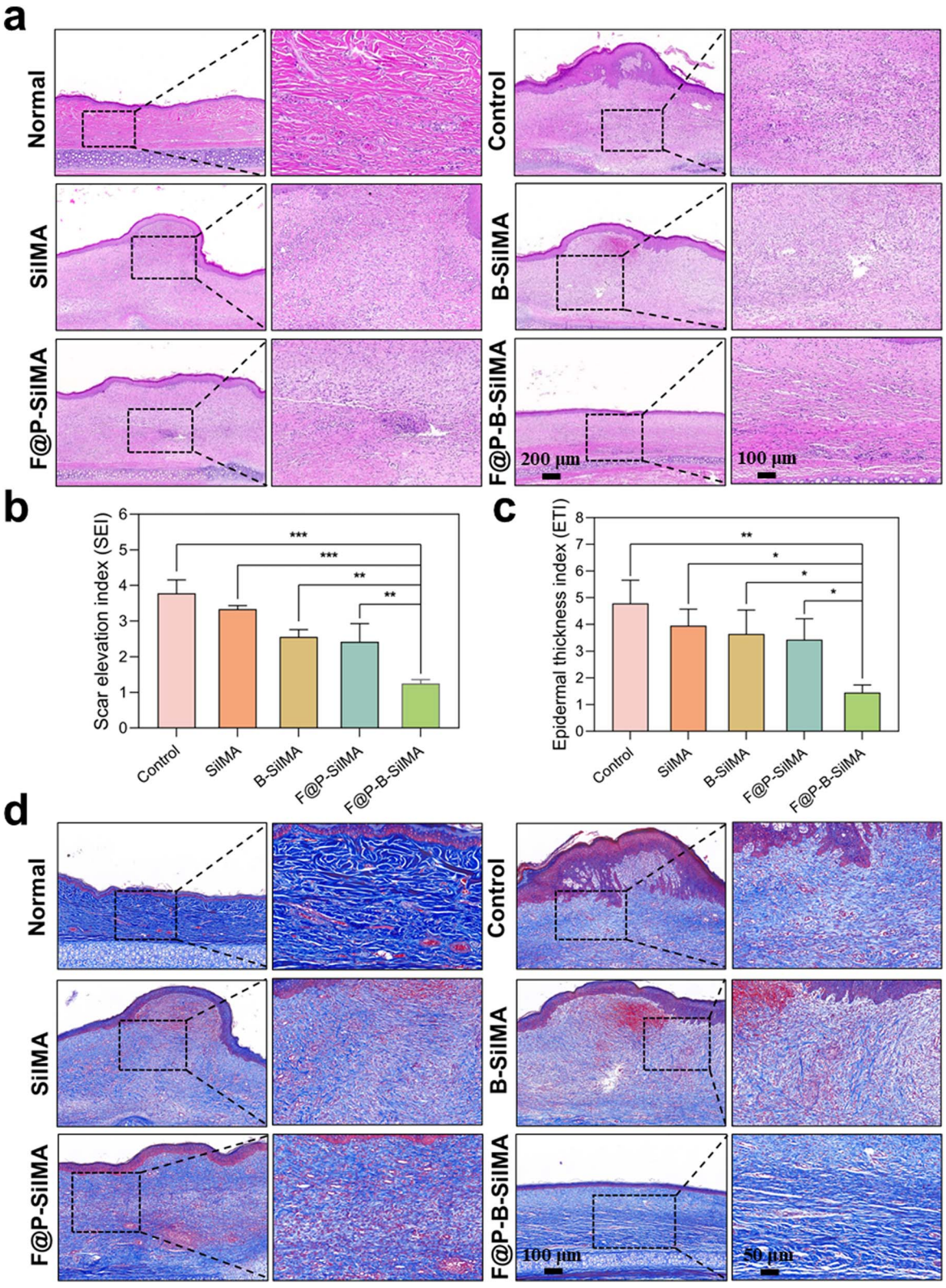


Fig. 5 Histological staining analysis of HS inhibition by F@P-B-SilMA. (a) H&E staining micrographs of the wound beds after different treatments. (b) SEI and (c) ETI results in different treatment groups. (d) Masson staining micrographs of the wound beds after different treatments. ***$P$ < 0.001, **$P$ < 0.01, and *$P$ < 0.05 indicate statistically significant difference between the compared groups.

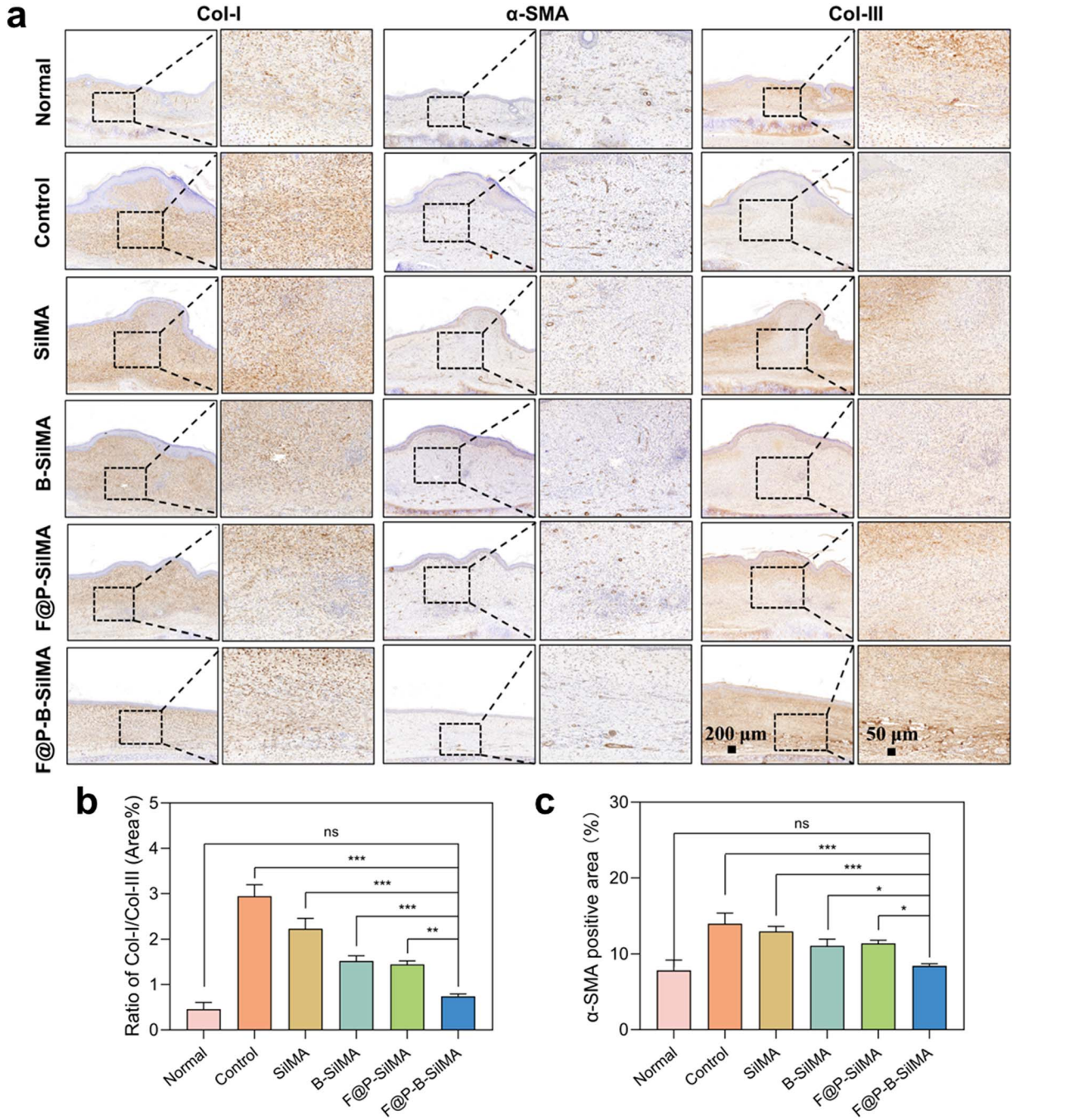


Fig. 6 IHC analysis of HS inhibition by F@P-B-SilMA. (a) IHC staining (Col-I, α-SMA, and Col-III) of the wound beds after different treatments. (b) Statistical analysis of the ratio of Col-I to Col-III (area%). (c) Statistical analysis of α-SMA positive area. "ns" indicates no significant difference between groups. ***$P$ < 0.001, **$P$ < 0.01, and *$P$ < 0.05 indicate statistically significant difference between the compared groups.

skin (Fig. 5a). Additionally, smaller values for SEI and ETI indicated reduced HS formation (Fig. S8).[48] Quantitative analysis using SEI and ETI revealed significantly lower values in the F@P-B-SilMA group, with SEI at 1.25 ± 0.09 and ETI at 1.45 ± 0.24, compared to the control group, which had SEI values of 3.78 ± 0.31 and ETI values of 4.78 ± 0.72. Similarly, the SilMA group showed SEI of 3.33 ± 0.08 and ETI of 3.95 ± 0.50, while the B-SilMA group showed SEI of 2.55 ± 0.17 and ETI of 3.63 ± 0.73. The F@P-SilMA group also demonstrated values of SEI at 2.41 ± 0.42 and ETI at 3.42 ± 0.64 (Fig. 5b and c). In addition, collagen fiber disorders are an important feature of HS.[49] Masson staining has revealed a distinct disorganization of collagen in HS, with normal tissue showing coarse and loosely arranged collagen fibers, while dense, nodular collagen deposition is observed in control samples (Fig. 5d). High-magnification imaging showed notable entanglement of collagen fibers and a disorganized distribution in control specimens. Therapeutic interventions led to substantial improvements in collagen

morphology and alignment when compared to controls. The F@P-B-SilMA group demonstrated reduced collagen deposition density, optimal fiber organization, and histological features closely resembling those of healthy tissue.

### 3.6 IHC analysis of F@P-B-SilMA for inhibition of HS

Subsequently, fibrosis-related protein expression was further studied using IHC in HS. The type of collagen fiber has a key influence on skin morphology, with Col-I and Col-III being the main components of adult skin tissue.[50] Col-I is thick and rigid, serving as the structural foundation of the skin. It is typically elevated in hyperplastic scars, which contribute to their stiffness. In contrast, Col-III is slimmer, providing softness and elasticity to the skin, and is usually present at lower levels in hyperplastic scars.[51,52] The results demonstrated that the F@P-B-SilMA treatment was more effective than other groups in reducing Col-I deposition and increasing Col-III deposition (Fig. 6a). Subsequent quantitative analysis of the Col-I/Col-III ratio confirmed that F@P-B-SilMA achieved a significantly greater reduction in this ratio, which consistent with therapeutic expectations (Fig. 6b). In addition,α-SMA, a marker of myofibroblast formation,[53] is known to be specifically overexpressed in HS.[54] α-SMA functions as a type of contractile cell that helps bind the edges of wounds together during skin tissue repair. It also triggers the deposition and alignment of collagen, which ultimately leads to the formation of HS.[55] The results indicated that F@P-B-SilMA was the most effective in suppressing the expression of α-SMA compared to other groups (Fig. 6a and c).

Compared with existing scar treatment methods, the F@P-B-SilMA system offers significant advantages. Traditional approaches primarily focus on inhibiting fibroblast proliferation but often overlook the quality of healed skin. In contrast, our composite not only achieves comparable wound closure rates but also significantly improves dermal architecture and reduces scar markers. Specifically, the biphasic release mechanism—with an initial rapid release of BTXA—helps control inflammation and suppress excessive scar formation, while the subsequent sustained release of 5-Fu from the microspheres continuously regulates fibroblast activity and promotes orderly arrangement of collagen fibers. Furthermore, this composite hydrogel system reduces the trauma and inconvenience associated with multiple injections, thereby improving patient compliance. Therefore, F@P-B-SilMA has great potential for controlling scar formation. Future studies will further explore the long-term efficacy of this system in large animal models and optimize its release kinetics to achieve more precise tissue regeneration.

## 4. Conclusion

In this study, we successfully developed an injectable F@P-B-SilMA hydrogel system to promote scarless wound healing. Our physicochemical analyses demonstrated that it has a three-dimensional porous structure that simulates the extracellular matrix. The hydrogel exhibits excellent tissue adhesion, deformability, and rheological properties, along with a degradation rate that aligns with the timelines of wound healing—collectively meeting essential criteria for effective wound dressings. Both *in vitro* and *in vivo* assessments confirmed its biocompatibility while highlighting its dual functionality: accelerating tissue repair and suppressing HS. In conclusion, the injectable F@P-B-SilMA composite hydrogel system offers a promising new approach for clinical treatments and has the potential to be developed as a dressing for scarless wound healing.

## Author contributions

Ming Xu: methodology, data curation, writing – original draft. Xihang Wang: methodology, data curation. Ziyi Zhou: investigation, methodology, data curation. Linna Wang: methodology. Jia Zhou: methodology. Xinyue Hu: methodology, data curation. Yuanfei Wang: supervision, funding acquisition, writing – review & editing. Tong Wu: conceptualization, resources, project administration, supervision, writing – review & editing, funding acquisition.

## Conflicts of interest

The authors declare that they have no known competing financial interests or personal relationships that could have appeared to influence the work reported in this paper.

## Data availability

All data generated or analyzed during this study are included in this article and its supplementary information (SI). The supplementary information file contains $IC_{50}$ values of HKFs and L929 cells for different concentrations of 5-Fu in scientific notation (Fig. S1), fluorescence micrographs of core–shell structured microspheres with red shell and green core layers (Fig. S2), a particle size distribution histogram of the microspheres (Fig. S3), rheological analysis data of the SilMA hydrogel (Fig. S4), histograms of pore size distribution for SilMA and F@P-B-SilMA hydrogels (Fig. S5), *in vitro* degradation profiles (Fig. S6), wound healing rates across different treatment groups at 3, 7, and 14 days (Fig. S7), and schematic representations illustrating the measurement methods for SEI and ETI (Fig. S8). See DOI: https://doi.org/10.1039/d5ra10037b.

## Acknowledgements

This research was supported by the Horizontal Project of Lanzhou Biotechnique Development Co., Ltd (BZ-KYZRKX-20230205-001), the National Natural Science Foundation of Shandong Province (ZR2024MH163), Qingdao Key Health Discipline Development Fund (2025-2027), and Shandong Provincial Key Medical and Health Discipline of Oral Medicine (2025-2027). The authors gratefully acknowledge the support provided by the Youth Science and Technology Innovation Team of Shandong Provincial Health Commission.

## References

1 T. Wu, X. Hou, J. Li, H. Ruan, L. Pei, T. Guo, Z. Wang, T. Ci, S. Ruan, Y. He, Z. He, N. Feng and Y. Zhang, Microneedle-Mediated Biomimetic Cyclodextrin Metal Organic Frameworks for Active Targeting and Treatment of Hypertrophic Scars, *ACS Nano*, 2021, **15**, 20087.

2 X. Lin and Y. Lai, Scarring Skin: Mechanisms and Therapies, *Int. J. Mol. Sci.*, 2024, **25**, 1458.

3 A. Bayat, D. A. McGrouther and M. W. Ferguson, Skin scarring, *Bmj*, 2003, **326**, 88.

4 H. Chen, K. Hou, Y. Wu and Z. Liu, Use of Adipose Stem Cells Against Hypertrophic Scarring or Keloid, *Front. Cell Dev. Biol.*, 2021, **9**, 823694.

5 F. S. Frech, L. Hernandez, R. Urbonas, G. A. Zaken, I. Dreyfuss and K. Nouri, Hypertrophic Scars and Keloids: Advances in Treatment and Review of Established Therapies, *Am. J. Clin. Dermatol.*, 2023, **24**, 225.

6 H. J. Lee and Y. J. Jang, Recent Understandings of Biology, Prophylaxis and Treatment Strategies for Hypertrophic Scars and Keloids, *Int. J. Mol. Sci.*, 2018, **19**, 711.

7 J. Q. Coentro, E. Pugliese, G. Hanley, M. Raghunath and D. I. Zeugolis, Current and upcoming therapies to modulate skin scarring and fibrosis, *Adv. Drug Delivery Rev.*, 2019, **146**, 37.

8 M. H. Gold, M. McGuire, T. A. Mustoe, A. Pusic, M. Sachdev, J. Waibel and C. Murcia, Updated international clinical recommendations on scar management: part 2-algorithms for scar prevention and treatment, *Dermatol. Surg.*, 2014, **40**, 825.

9 Y. Zhang, Z. Zhou, N. Liu, J. Wang, Q. Guo, Y. You, K. Mao, Y. Wang, W. Zhang and T. Wu, Curcumin-loaded PLGA microparticles integrated with ZnO/GelMA hydrogel microneedles for infectious wound healing and reduction of hypertrophic scars, *J. Nanobiotechnol.*, 2025, **23**, 455.

10 P. Sun, X. Lu, H. Zhang and Z. Hu, The Efficacy of Drug Injection in the Treatment of Pathological Scar: A Network Meta-analysis, *Aesthet. Plast. Surg.*, 2021, **45**, 791.

11 Y. Li, D. Zhang, B. Hang and H. Wang, The Efficacy of Combination Therapy Involving Excision Followed by Intralesional 5-Fluorouracil and Betamethasone, and Radiotherapy in the Treatment of Keloids: A Randomized Controlled Trial, *Clin., Cosmet. Invest. Dermatol.*, 2022, **15**, 2845.

12 S. F. Ekstein, S. P. Wyles, S. L. Moran and A. Meves, Keloids: a review of therapeutic management, *Int. J. Dermatol.*, 2021, **60**, 661.

13 S. A. Ismail, N. H. K. Mohammed, M. Sotohy and D. A. E. Abou-Taleb, Botulinum toxin type A *versus* 5-Fluorouracil in treatment of keloid, *Arch. Dermatol. Res.*, 2021, **313**, 549.

14 Y.-X. Wang, Y. Wang, Q. Zhang and R.-D. Zhang, Current Research of Botulinum Toxin Type A in Prevention and Treatment on Pathological Scars, *Dermatol. Surg.*, 2023, **49**, S34–S40.

15 M. Rosales Santillan, D. Ozog and W. Wu, Using Neuromodulators to Improve Scar Formation, Keloids, Rosacea, and Antiaging, *Dermatol. Surg.*, 2024, **50**, S91–S96.

16 Y.-p Zou, X.-f Shan, J.-x Qiu, L.-n Wang, R.-l Xiang and Z.-g Cai, Botulinum toxin type A inhibits M1 macrophage polarization by deactivation of JAK2/STAT1 and IκB/NFκB pathway and contributes to scar alleviation in aseptic skin wound healing, *Biomed. Pharmacother.*, 2024, **174**, 116468.

17 T. Searle, F. Al-Niaimi and F. R. Ali, 5-Fluorouracil in Dermatology: The Diverse Uses Beyond Malignant and Premalignant Skin Disease, *Dermatol. Surg.*, 2021, **47**, e66.

18 Y. Li, Q. Sun, L. Hao, H. Shan, Z. Jiang, Y. Wang, Z. Chen, W. Zhu and S. Zhao, Liposomes Loaded with 5-Fluorouracil Can Improve the Efficacy in Pathological Scars, *Int. J. Nanomed.*, 2024, **19**, 7353.

19 F. A. Khalid, M. Y. Mehrose, M. Saleem, M. A. Yousaf, A. M. Mujahid, S. U. Rehman, S. Ahmad and M. N. Tarar, Comparison of efficacy and safety of intralesional triamcinolone and combination of triamcinolone with 5-fluorouracil in the treatment of keloids and hypertrophic scars: Randomised control trial, *Burns*, 2019, **45**, 69.

20 D. B. Longley, D. P. Harkin and P. G. Johnston, 5-fluorouracil: mechanisms of action and clinical strategies, *Nat. Rev. Cancer*, 2003, **3**, 330.

21 J. Wang, Z. Zhou, X. Zhang, M. Fu, K. Fang, Y. Wang and T. Wu, One-Step Manufacture and Crosslinking of Gelatin/Polygonum sibiricum Polysaccharide Bioactive Nanofibrous Sponges for Rapid Hemostasis and Infected Wound Healing, *Adv. Fiber Mater.*, 2025, **7**, 1148.

22 L. Hong, P. Qiu, S. Niu, Q. Chen, X. Lu, F. Chen, M. Wen, N. Yu and Z. Chen, On-Site Electrospinning Nanofiber Membranes Incorporating V-Shaped Organic Semiconductors for Multifunctional Diabetic Wound Dressing, *Adv. Fiber Mater.*, 2024, **6**, 1413.

23 N. Liu, Z. Zhou, X. Zhang, Q. Guo, Y. Yan, M. Fu, Y. Wang, Y. Wang and T. Wu, Carboxymethyl chitosan hydrogel reinforced by endothelial cell derivatives for angiogenesis and full-thickness wound healing, *Mater. Des.*, 2025, **260**, 115242.

24 L. Zhang, Y. Yang, J. Wang, H. Zhang, Z. Zhang and B. Guo, A Portable, Sprayable, Highly Malleable, Elastic, and Hydrophobic Antibacterial Fibrous Wound Dressing for Infected Wound Healing, *Adv. Fiber Mater.*, 2025, **7**, 528.

25 Z. Ling, J. Deng, Z. Zhang, H. Sui, W. Shi, B. Yuan, H. Lin, X. Yang, J. Cao, X. Zhu and X. Zhang, Spatiotemporal manipulation of L-arginine release from bioactive hydrogels initiates rapid skin wound healing accompanied with repressed scar formation, *Appl. Mater. Today*, 2021, **24**, 101116.

26 Y. Shen, G. Xu, H. Huang, K. Wang, H. Wang, M. Lang, H. Gao and S. Zhao, Sequential Release of Small Extracellular Vesicles from Bilayered Thiolated Alginate/Polyethylene Glycol Diacrylate Hydrogels for Scarless Wound Healing, *ACS Nano*, 2021, **15**, 6352.

27 M. Wang, C. Wang, M. Chen, Y. Xi, W. Cheng, C. Mao, T. Xu, X. Zhang, C. Lin, W. Gao, Y. Guo and B. Lei, Efficient Angiogenesis-Based Diabetic Wound Healing/Skin

Reconstruction through Bioactive Antibacterial Adhesive Ultraviolet Shielding Nanodressing with Exosome Release, *ACS Nano*, 2019, **13**, 10279.

28 Z. Zhang, Y. Zhang, W. Li, L. Ma, E. Wang, M. Xing, Y. Zhou, Z. Huan, F. Guo and J. Chang, Curcumin/Fe-SiO2 nano composites with multi-synergistic effects for scar inhibition and hair follicle regeneration during burn wound healing, *Appl. Mater. Today*, 2021, **23**, 101065.

29 J. K. Sahoo, O. Hasturk, T. Falcucci and D. L. Kaplan, Silk chemistry and biomedical material designs, *Nat. Rev. Chem.*, 2023, **7**, 302.

30 L. Xu, Z. Zhang, A. M. Jorgensen, Y. Yang, Q. Jin, G. Zhang, G. Cao, Y. Fu, W. Zhao, J. Ju and R. Hou, Bioprinting a skin patch with dual-crosslinked gelatin (GelMA) and silk fibroin (SilMA): An approach to accelerating cutaneous wound healing, *Mater. Today Bio*, 2023, **18**, 100550.

31 S. H. Kim, Y. K. Yeon, J. M. Lee, J. R. Chao, Y. J. Lee, Y. B. Seo, M. T. Sultan, O. J. Lee, J. S. Lee, S. I. Yoon, I. S. Hong, G. Khang, S. J. Lee, J. J. Yoo and C. H. Park, Precisely printable and biocompatible silk fibroin bioink for digital light processing 3D printing, *Nat. Commun.*, 2018, **9**, 1620.

32 X. Wu, M. Zhou, F. Jiang, S. Yin, S. Lin, G. Yang, Y. Lu, W. Zhang and X. Jiang, Marginal sealing around integral bilayer scaffolds for repairing osteochondral defects based on photocurable silk hydrogels, *Bioact. Mater.*, 2021, **6**, 3976.

33 W. Zhao, J. Li, K. Jin, W. Liu, X. Qiu and C. Li, Fabrication of functional PLGA-based electrospun scaffolds and their applications in biomedical engineering, *Mater. Sci. Eng., C*, 2016, **59**, 1181.

34 X. Zhang, R. Zhu, X. Wang, H. Wang, Z. Xu, Y. Wang, D. Quan and L. Shen, Core-Shell Microspheres Prepared Using Coaxial Electrostatic Spray for Local Chemotherapy of Solid Tumors, *Pharmaceutics*, 2024, **16**, 45.

35 T. T. Dongsar, T. S. Dongsar, N. Gupta, W. H. Almalki, A. Sahebkar and P. Kesharwani, Emerging potential of 5-Fluorouracil-loaded chitosan nanoparticles in cancer therapy, *J. Drug Delivery Sci. Technol.*, 2023, **82**, 104371.

36 N. Atefi, M. A. Jafari, M. Roohaninasab, A. Dehghani, A. Jafarzadeh, S. B. Peighambari, A. Peighambari and A. Goodarzi, Evaluating the effectiveness and safety of pulsed dye laser alone, the combination of pulsed dye laser and botulinum toxin type A, and the combination of pulsed dye laser and triamcinolone injection in the treatment of hypertrophic and keloid scars: a three-arm randomized controlled clinical trial, *Lasers Med. Sci.*, 2025, **40**, 92.

37 S. P. Nischwitz, K. Rauch, H. Luze, E. Hofmann, A. Draschl, P. Kotzbeck and L. P. Kamolz, Evidence-based therapy in hypertrophic scars: an update of a systematic review, *Wound Repair Regen.*, 2020, **28**, 656.

38 E. Shaarawy, R. A. Hegazy and R. M. Abdel Hay, Intralesional botulinum toxin type A equally effective and better tolerated than intralesional steroid in the treatment of keloids: a randomized controlled trial, *J. Cosmet., Dermatol.*, 2015, **14**, 161.

39 Y. X. Wang, Y. Wang, Q. Zhang and R. D. Zhang, Current Research of Botulinum Toxin Type A in Prevention and Treatment on Pathological Scars, *Dermatol. Surg.*, 2023, **49**, S34.

40 Z. Xiao and G. Qu, Effects of botulinum toxin type a on collagen deposition in hypertrophic scars, *Molecules*, 2012, **17**, 2169.

41 H. Jafari, K. V. Bernaerts, G. Dodi and A. Shavandi, Chitooligosaccharides for wound healing biomaterials engineering, *Mater. Sci. Eng., C*, 2020, **117**, 111266.

42 Q. Hu, N. Xie, K. Liao, J. Huang, Q. Yang, Y. Zhou, Y. Liu and K. Deng, An injectable thermosensitive Pluronic F127/hyaluronic acid hydrogel loaded with human umbilical cord mesenchymal stem cells and asiaticoside microspheres for uterine scar repair, *Int. J. Biol. Macromol.*, 2022, **219**, 96.

43 O. Kloeters, A. Tandara and T. A. Mustoe, Hypertrophic scar model in the rabbit ear: a reproducible model for studying scar tissue behavior with new observations on silicone gel sheeting for scar reduction, *Wound Repair Regen.*, 2007, **15**(1), S40.

44 S. Wen, H. Zhao, Y. Zhang, D. Cao, M. Liu, H. Yang and W. Zhang, Multifunctional Nanofiber Membranes Constructed by Microfluidic Blow-Spinning to Inhibit Scar Formation at Early Intervention Stage, *ACS Appl. Mater. Interfaces*, 2024, **16**, 53042.

45 W. Weng, S. He, H. Song, X. Li, L. Cao, Y. Hu, J. Cui, Q. Zhou, H. Peng and J. Su, Aligned Carbon Nanotubes Reduce Hypertrophic Scar *via* Regulating Cell Behavior, *ACS Nano*, 2018, **12**, 7601.

46 M. Gholipourmalekabadi, S. Khosravimelal, Z. Nokhbedehghan, M. Sameni, V. Jajarmi, A. M. Urbanska, H. Mirzaei, M. Salimi, N. P. S. Chauhan, M. Mobaraki, R. L. Reis, A. Samadikuchaksaraei and S. C. Kundu, Modulation of Hypertrophic Scar Formation Using Amniotic Membrane/Electrospun Silk Fibroin Bilayer Membrane in a Rabbit Ear Model, *ACS Biomater. Sci. Eng.*, 2019, **5**, 1487.

47 H. Hong, Y. B. Seo, D. Y. Kim, J. S. Lee, Y. J. Lee, H. Lee, O. Ajiteru, M. T. Sultan, O. J. Lee, S. H. Kim and C. H. Park, Digital light processing 3D printed silk fibroin hydrogel for cartilage tissue engineering, *Biomaterials*, 2020, **232**, 119679.

48 M. Gholipourmalekabadi, A. M. Seifalian, A. M. Urbanska, M. D. Omrani, J. G. Hardy, Z. Madjd, S. M. Hashemi, H. Ghanbarian, P. Brouki Milan, M. Mozafari, R. L. Reis, S. C. Kundu and A. Samadikuchaksaraei, 3D Protein-Based Bilayer Artificial Skin for the Guided Scarless Healing of Third-Degree Burn Wounds in Vivo, *Biomacromolecules*, 2018, **19**, 2409.

49 Z. Zhang, C. Fang, J. Ke, Y. Li, M. Duan, J. Ren and C. Wang, Microneedle drug delivery system based on hyaluronic acid for improving therapeutic efficiency of hypertrophic scars, *Int. J. Biol. Macromol.*, 2025, **297**, 139790.

50 L. Ding, H. Lin, Z. Yang, P. Zhang and X. Chen, Polycaprolactone/gelatin-QAS/bioglass nanofibres accelerate diabetic chronic wound healing by improving dysfunction of fibroblasts, *Int. J. Biol. Macromol.*, 2024, **283**, 136699.

51 H. Y. Kim, H. Y. Im, H. K. Chang, H. D. Jeong, J. H. Park, H. I. Kim, H. S. Yi and Y. S. Kim, Correlation between Collagen Type I/III Ratio and Scar Formation in Patients Undergoing Immediate Reconstruction with the Round Block Technique after Breast-Conserving Surgery, *Biomedicines*, 2023, **11**, 1089.

52 J. Jin, H. Li, Z. Chen, Q. Liu, J. Chen, Z. Tao, X. Hong, Y. Ding, Y. Zhou, A. Chen, X. Zhang, K. Lv, L. Zhu and S. Zhu, Endocytosis-mediated healing: recombinant human collagen type III chain-induced wound healing for scar-free recovery, *Regener. Biomater.*, 2025, **12**, rbae149.

53 A. V. Shinde, C. Humeres and N. G. Frangogiannis, The role of α-smooth muscle actin in fibroblast-mediated matrix contraction and remodeling, *Biochim. Biophys. Acta, Mol. Basis Dis.*, 2017, **1863**, 298.

54 J. Q. Coentro, E. Pugliese, G. Hanley, M. Raghunath and D. I. Zeugolis, Current and upcoming therapies to modulate skin scarring and fibrosis, *Adv. Drug Delivery Rev.*, 2019, **146**, 37.

55 G. C. Gurtner, S. Werner, Y. Barrandon and M. T. Longaker, Wound repair and regeneration, *Nature*, 2008, **453**, 314.